

## Automated mapping of linear dunefield morphometric parameters from remotely-sensed data



M.W. Telfer\*, R.M. Fyfe, S. Lewin

School of Geography, Earth and Environmental Science, Plymouth University, Drake Circus, Plymouth, Devon PL4 8AA, UK

### ARTICLE INFO

#### Article history:

Available online 14 April 2015

#### Keywords:

Dunes  
Dunefield  
Remote sensing  
Pattern analysis  
Edge detection  
Complex systems

### ABSTRACT

Linear dunes are among the world's most common desert dune types, and typically occur in dunefields arranged in remarkably organized patterns extending over hundreds of kilometers. The causes of the patterns, formed by dunes merging, bifurcating and terminating, are still poorly understood, although it is widely accepted that they are emergent properties of the complex system of interactions between the boundary layer and an often-vegetated erodible substrate. Where such dunefields are vegetated, they are typically used as extensive rangeland, yet it is evident that many currently stabilized dunefields have been reactivated repeatedly during the late Quaternary. It has been suggested that dunefield patterning and the temporal evolution of dunefields are related, and thus there is considerable interest in better understanding the boundary conditions controlling dune patterning, especially given the possibility of reactivation of currently-stabilized dunefields under 21st century climate change. However, the time-consuming process of manual dune mapping has hampered attempts at quantitative description of dunefield patterning.

This study aims to develop and test methods for delineating linear dune trendlines automatically from freely-available remotely sensed datasets. The highest resolution free global topographic data presently available (Aster GDEM v2) proved to be of marginal use, as the topographic expression of the dunes is of the same order as the vertical precision of the dataset (~10 m), but in regions with relatively simple patterning it defined dune trends adequately. Analysis of spectral data (panchromatic Landsat 8 data) proved more promising in five of the six test sites, and despite poor panchromatic signal/noise ratios for the sixth site, the reflectance in the deep blue/violet (Landsat 8 Band 1) offers an alternative method of delineating dune pattern. A new edge detection algorithm (Linear Dune Optimized edge detection; LIDO) is proposed, based on Sobel operators with directional filtering and topologically-constrained recursion to optimize the inclusion of marginal zones. The method offers the potential for rapid quantitative mapping of linear dunefield patterning, providing validation data for modeling studies, and offering for the first time the ability to readily remap dunefields to assess dune reorganization at the dunefield scale.

© 2015 Elsevier B.V. All rights reserved.

### 1. Introduction

Linear dunefields present some of the most strikingly-organized landforms on earth. Individual dunes may only be ~10 m high and ~100 m wide, but can be ~10–100 km in length and major dunefields contain many thousands of individual dunes, often remarkably evenly spaced. Within this regularity, however, there can also be much subtle variation. Dunes may bifurcate or coalesce (with respect to the net transporting wind vector) and they may initiate or terminate. Such 'defects' result in patterning within the dunefield; that is, the semi-regular but spatially variable arrangement of dunes, interdunes and defects (e.g. Fig. 1). Such patterning

is now widely accepted to be the result of self-organization within the complex system of the aeolian transport environment, comprising a turbulent atmospheric boundary layer and a (usually vegetated) erodible, particulate substrate. Patterning is thus an emergent property influenced by regional and/or site-specific boundary conditions which evolves through interactions of individual dunes (Werner, 1995; Werner and Kocurek, 1997, 1999). Although the broad influence of some boundary conditions (e.g. wind regime) is fairly well understood, the variance in naturally-observed patterning exceeds that generated from numerical modeling, implying that the nature of some boundary conditions is still poorly understood (Ewing and Kocurek, 2010; Kocurek et al., 2010). Understanding the dynamic response of linear dunefields to changing boundary conditions may prove crucial to understanding the landscape response to modern-day climate

\* Corresponding author.

E-mail address: [matt.telfer@plymouth.ac.uk](mailto:matt.telfer@plymouth.ac.uk) (M.W. Telfer).

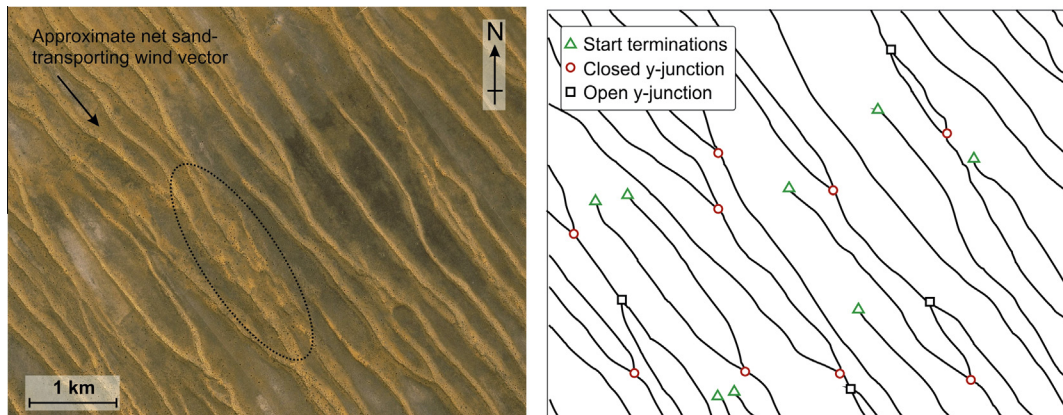


**Fig. 1.** An example of manual interpretation of dune morphometric parameters from a CNES/SPOT image, courtesy of Google Earth™ (imagery date 4/10/2013, retrieved 14/2/2014), of the southwestern Kalahari (image centered on 25.672°S, 19.264°E). Note the region in the dashed line, in which the dune trends are less clear, and interpretation of the image is less likely to be subjective.

change, which has been suggested as a driver of widespread dune reactivation in desert-marginal regions in the 21st century (Thomas et al., 2005).

A key challenge in studying dunefield patterning is the time-consuming process of measuring the key morphometric parameters (e.g. frequency of bifurcations) at the dunefield scale. This has traditionally been done by manual interpretation of aerial imagery, but the intensive nature of this has meant that it has been limited to either small dunefields (e.g. Derickson et al., 2008), sampled regions from large dunefields (e.g. Al-Masrahy and Mountney, 2013; Bullard et al., 1995) or at a large scale, but in a qualitative manner (e.g. Fitzsimmons, 2007). The absence of quantitative metrics at the dunefield scale has been noted as a limitation in past studies. An ideal approach would thus be a (semi-)automated methodology to enable quantitative, systematic, objective and large-scale morphometric analysis. Such methods would also facilitate repeat temporal analyses with a focus on change detection (Varma et al., 2014).

The recent increase in the availability of global, high resolution remotely-sensed datasets offers an important resource for the study of aeolian environments (Hugenholz et al., 2012). For instance, digital elevation data has been used to study dune orientation and spacing by means of Fourier transforms (Cazenave et al., 2013), and the feasibility of extracting some dune metrics, such as orientation, by automated methods has been demonstrated (Varma et al., 2012). Some studies have demonstrated the utility of global elevation datasets in morphometric analysis of megadunes, where topographic expression is >20–30 m (e.g. Bubenzer and Bolten, 2008). The swathes of linear dunes that characterize many of the world's semi-arid desert marginal regions, however, are typically considerably smaller than this, with crest heights of ~10 m typical for the Australian and southern African dunefields (Lancaster, 1995). This paper thus aims to investigate and test methods for the automation of dune morphometric analyses in linear dunefields, using freely-available remotely sensed data within a Geographical Information Systems (GIS) framework.

Two broad possibilities exist for delineating dunes from remotely-sensed data. Firstly, it might be possible to define them on the basis of their spectral characteristics (i.e. either their colour, as is done by manual interpretation of imagery, or some aspect of the non-visible spectrum). Such an approach has been demonstrated by Al-Dabi et al. (1997). Secondly, they might be identified as local positive topographic anomalies at an appropriate scale from elevation data (e.g. Hugenholz and Barchyn, 2010). Either approach towards the goal of automated delineation of dune trends faces a number of challenges, some of which are in common

with manual methods, and some of which are more specific to the automation of the process. Amongst these are:

- (1) Defining suitable ontologies for discrete landforms and their inter-relationships from representations of the landscape, and defining suitable objective rules for classifying marginal interpretations.
- (2) Discriminating between variance in elevation or spectral data at scales appropriate to identifying landforms (e.g. removing regional trends in elevation data or managing different illumination aspects and elevations in the visible spectrum).
- (3) Discriminating dunes from other linear topographical or spectral features (e.g. roads, drainages, etc.).
- (4) Providing quantitative estimates of uncertainty of the output.

### 1.1. Ontologies of a dunefield: Dune morphometry and topology

The spatial patterning of a dunefield is defined by the presence, frequency and arrangement of a number of basic parameters, which can be quantified in planform analysis of dune morphology. Most studies have used similar variables. Bullard et al. (1995) identified Y-junctions, termini, orientation range, and wavelength as the key parameters describing dune morphometry, and Werner and Kocurek (1997) classified defects as junctions and terminations (Fig. 1). Ewing et al. (2006) identified crest length, crest orientation, dune spacing (i.e. wavelength) and defect density as the key parameters. Within linear dunefields, where the dunes are oriented broadly longitudinally to the regional net sand-transporting wind vector, defects can be further sub-divided relative to the wind orientation. Henceforth, in this study the terminology of Thomas and Shaw (1991) is adopted, and 'closed Y-junction' is used to describe the situation where two dunes merge downwind and 'open Y-junction' is introduced where a dune bifurcates downwind. Terminations can similarly be described as start-terminations and end-terminations.

However, the challenges of object-based ontologies of dune geomorphology have been discussed by Hugenholz et al. (2012), and a number of aspects of linear dunefield morphology complicate the ontologies of defining linear dunes. For instance, linear dunes may have smaller linear dunes superimposed upon them (e.g. Dong et al., 2010; Lancaster et al., 2002). The single, well-defined crests may also be interrupted by blow-outs (Hesse and Simpson, 2006), or in cases which are generally rare but locally abundant (e.g. Great Sandy Desert, Australia), linear dunes may

have multiple crestlines (Hesse, 2010). For the purposes of this study, the formal ontology of a dune used here is thus a linear feature with a minimum length (here 150 m; see Section 3.4 for the derivation of this threshold), whose orientation lies within a specified range. Linear features are defined either on the basis of topological position or spectral characteristics. Start and end nodes of polylines are used to define terminations or junctions, dependent on topological relationship between polylines.

## 2. Morphometric and spectral analysis methods for identifying dune topology from remotely-sensed data

This paper develops methodologies for analyzing freely-available global data, which limits the choice of datasets to be used. The very high-resolution data familiar to many from widely-used applications such as Google Earth™ are not freely available in a form that allows for analysis. The spatial resolution of Google Earth™ imagery is spatially and temporally very variable, but in some instances can be sub-meter; the images used in this study are typically ~1 m in resolution. Morphometric approaches to delimiting dune topology rely on high resolution topographic datasets. Presently, the highest resolution freely-available global topographic dataset available is the Aster GDEM v2 (NASA/METI, 2011), offering 30 m horizontal resolution and thus likely to be suitable for mapping dunes which are typically around 100 m wide. However, the data have an estimated absolute vertical uncertainty of ~6 m for low-relief open terrain (Tachikawa et al., 2011). Until the advent of higher precision global datasets (e.g. Krieger et al., 2007), any attempt at automated morphometric analyses is thus challenged by seeking to identify topographic features of the same order of magnitude as the uncertainty in the vertical resolution of the data. The 1 arc-second version of the Shuttle Radar Topographic Mission (SRTM) was released free of charge for Africa during the late stages of the preparation of this manuscript, and offers the same precision; global coverage will be released during 2015. The relative vertical accuracy of these data should offer an alternative to the Aster GDEM.

Remotely sensed multi-spectral data offer a complementary approach to topographic variance. Perhaps the most powerful freely-available spectral data come from the Landsat 8 platform, which was launched in 2013, and carries the Operational Land Imager (OLI) sensor, along with a lower spatial resolution Thermal Infrared Sensor (TIRS). These data are freely distributed by the Land Processes Distributed Active Archive Center (LP DAAC), located at USGS/EROS, Sioux Falls, South Dakota, US (<http://lpdaac.usgs.gov>). The OLI is comparable to the more familiar Enhanced Thematic Mapper Plus (ETM+) sensor carried by Landsat 7, which has been operational since 1999. Data are collected from nine spectral bands, ranging from violet (a new band compared to ETM+ at 0.43–0.45 μm) to short-wave infrared (2.11–2.29 μm), including a panchromatic band (0.50–0.68 μm) with enhanced spatial resolution (15 m). Recent cloud-free scenes were selected for each of the sample sites.

Whether using topographic or spectral data, there are four key stages of analysis. First, variability in elevation/spectral signature at scales inappropriate to the dunes (e.g. regional trends) must be accounted for. Second, noise within the data must be removed, for instance, pixel-level uncertainties in the data or sub-dune-scale entities. The third stage is to apply some form of binary classification to define dune/non-dune pixels. Fourth, dune trend lines (in essence, the dune crestline) must be vectorized to enable identification of defects and quantitative pattern analysis.

Six sites of 15 km by 10 km were selected from four dunefields to develop and test the methodology of discerning dune crests from remotely sensed data. Three are from the southwestern

**Table 1**

Sites selected for use as training sets to test methods of automated dune crest delineation, with position on the top-left corner of the image given.

Name	Lat	Long	Pattern complexity	Approximate net sand-transporting wind direction
SW Kalahari North	-24.62°S	18.95°E	Low	N → S
SW Kalahari Central	-25.84°S	19.53°E	Medium	N → S
SW Kalahari South	-26.41°S	20.31°E	High	NW → SE
Great Sandy Desert	-20.16°S	123.87°E	Medium	E → W
Simpson	-25.01°S	136.96°E	Low/Medium	S → N
Strzelecki	-28.61°S	140.50°E	Medium/High	SW → NE

Kalahari, and one each from Australia's Great Sandy, Simpson and Strzelecki deserts (Table 1). Sites were selected to offer a range of conditions to test the applicability of automated mapping under a wide range of parameters (e.g. dune size, pattern complexity, vegetation cover, lithology, etc.). Dune patterning was manually digitized from Google Earth™ imagery to provide a benchmark against which to assess the success of the methods employed. With each dataset, a qualitative, visual inspection of Google Earth™ imagery preceded further analysis with ArcGIS 10.2. The qualitative inspection was necessary to provide estimates of overall dune orientation and size, in order to scale focal filters appropriately, and where necessary, to parameterize relevant directional filters. A series of spatial filters were tested on the raster data in order to produce the best binary (i.e.: dune/not dune) classification possible. Initially, relatively simple methods were tested, such as a focal range filter using the Moore neighbourhood of the target cell (i.e., a radius of 15 m for Landsat8, and 30 m for Aster GDEM) to identify localized variance in reflectance/topography, and a variety of high-pass/low-pass mean filter combinations at different radii to filter dune-scale from larger variance.

More complex filter approaches included knowledge of dune orientation established during the visual inspection. Initial attempts to exploit the preferential orientation of linear dunes used a combination of directionally weighted convolution kernel filters at 45° intervals, defined such that  $W = V^2 + V_{-45} + V_{+45}$  where  $W$  is the weighted raster score,  $V$  is the output of a binary kernel filter of the form [0,0,0;1,1,1;0,0,0] when the dominant dune direction is approximated best as East–West, and  $V_{+45}$  and  $V_{-45}$  are the according kernel filters for the ordinal directions either side of the primary orientation. The Canny edge detection algorithm (Canny, 1986) was also tested. This is a widely used, multi-stage edge detection algorithm which initially uses a Gaussian smoothing filter and then Sobel operators (a weighted kernel of the form [-1,-2,-1;0,0,0;1,2,1] in the  $y$  plane, and its rotation through 90° in the  $x$  plane) to define gradient magnitude and direction (Sobel and Feldman, 1968). Local maxima in gradient are identified in each of the ordinal directions to reduce the edge to a single pixel's width ('non-maxima suppression'), and then variable thresholds are used recursively to identify strong edges. Weaker but connected edges remain, and are incorporated into the final image.

When the limitations of each of these methods to successfully define dune edges in all of the six test sites became apparent, attention was focused on defining a new methodology, details of which are provided in Section 3.4 below.

## 3. Results and Discussion

### 3.1. Topographical data

The results from the Aster GDEM are mixed (Fig. 2). This is a consequence of use of a dataset which has vertical uncertainties of the same order as the features to be delineated. Where the dunes are relatively well-defined and the patterning simple, even low

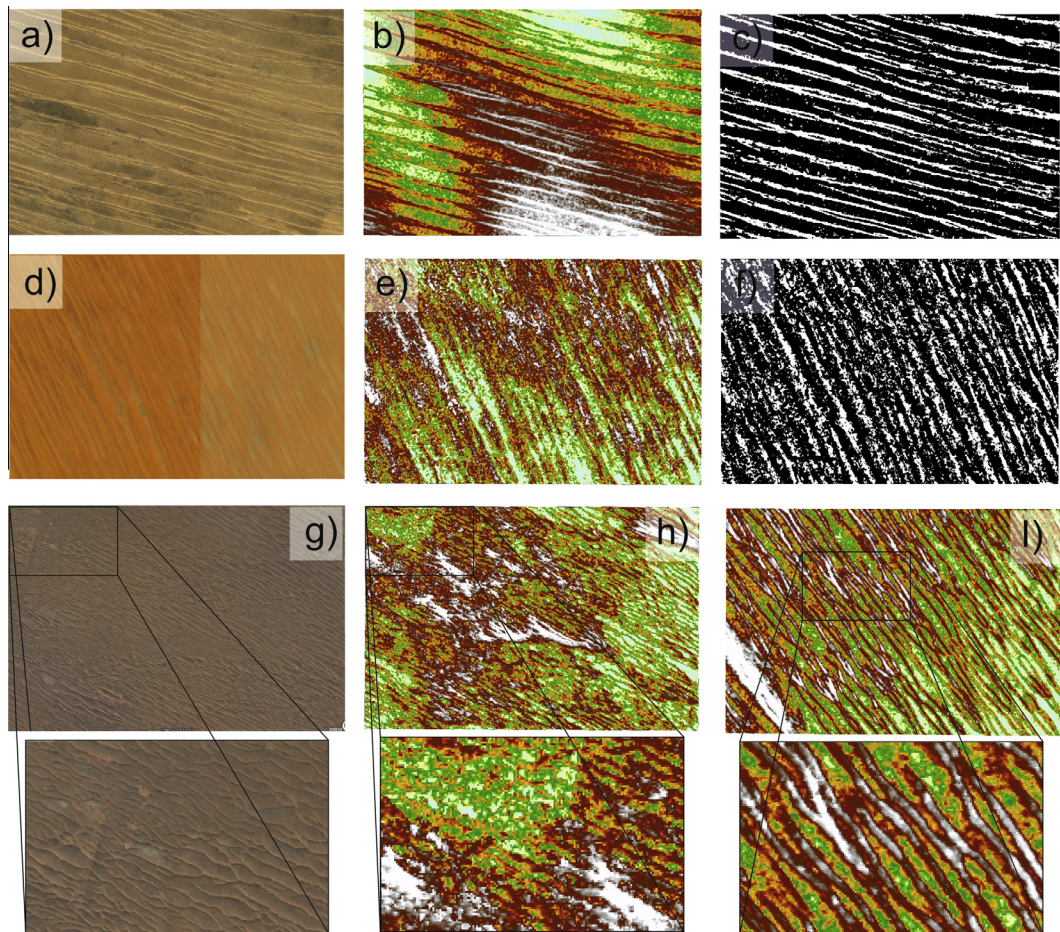


**Fig. 2.** SPOT (via the Google Earth™ platform) and Aster GDEM data for the four of the sites investigated. (a) SPOT imagery for the Great Sandy Desert, compared with (b) the ASTER GDEM elevation model and (c) the ASTER GDEM filtered with a high-pass/low-pass combination and reclassified to a binary output. (d) SPOT image for the Simpson test site, and (e) and (f) reveals that here the ASTER GDEM performs poorly in delineating dunes, using the same filtering methodology as above. The high degree of complexity for the South Kalahari site is shown in (g) with the inset providing detail. At this level of pattern complexity, the ASTER GDEM is unable to define individual dune crests, as seen in (h) and accompanying inset. Nonetheless, where patterning is less complex (in i), the central southwestern Kalahari site), dune trends and defects to patterning are well represented despite the dune height being only ~10 m. All scenes have a field of view 15 × 10 km, with insets 5 × 2.9 km.

relief (~10 m) landforms can be well described (e.g. Kalahari North and Central, Great Sandy Desert; Fig. 2a–c and i). In cases where the patterning is more complex and mean interdune spacing is on the order of 100–200 m (e.g. Kalahari South and Strzelecki; Fig. 2g and h) the patterning is largely lost. The dunes of the southern Simpson desert are also poorly delineated (Fig. 2d–f), despite relatively simple patterning (the interdune spacing is approximately 200–400 m) and similar relief landforms (Lancaster, 1995). The reasons for the poor performance of the ASTER GDEM in the Simpson desert compared to morphologically similar dunes in, say, the central southwestern Kalahari are not immediately clear. The elevation model for this region is typically derived from ‘stacks’ of five to seven individual ASTER scenes, and only a very few isolated pixels in the western part of the test image fall below the threshold of three stacks which is regarded as likely to result in anomalous results (Tachikawa et al., 2011). There are, however, noted issues with noise and error within the Aster GDEM from comparable low-relief dryland landscapes (e.g. Athmania and Achour, 2014), which may be contributing to both random and systematic errors.

Whilst the performance of the ASTER GDEM to delineate dunes whose topographic expression is of a similar magnitude to the expected error in the data is impressive in some areas, in other regions this application is clearly pushing the data beyond its reasonable usage. It may prove useful locally in mapping dunefields of

even moderate relief (~10–15 m), but it cannot be considered globally applicable.

### 3.2. Spectral data

With the OLI (i.e. Landsat 8) data, only the visible and panchromatic bands are of an appropriate resolution to attempt delineation of dune crests, as the spatial resolution of the infrared bands (100 m) is too coarse to produce useful results. However, the panchromatic (0.52–0.90 μm) band with 15 m spatial resolution reveals sufficient detail to characterize even the most densely patterned dunefields within the survey areas. Crucially, as dunes are here being identified by the differing spectral characteristics of the shadowed and sunlit sides of the dune crest, solar elevation proves very significant in providing useful images from which to work. As Landsat 8 is sun-synchronous, this essentially equates to seasonality of the image, with austral winter images providing much clearer delineation of the dune crest due to the lower angle of illumination and sharper contrasts (Fig. 3a and b). The additional resolution offered by the panchromatic band (15 m) compared to the other optical bands (30 m) is crucial, and there was generally no further benefit for dune detection from, for instance, composite RGB images, even when pan-sharpened.

Although dune trends are broadly evident in all of the study areas, a specific challenge emerges in areas where vegetation

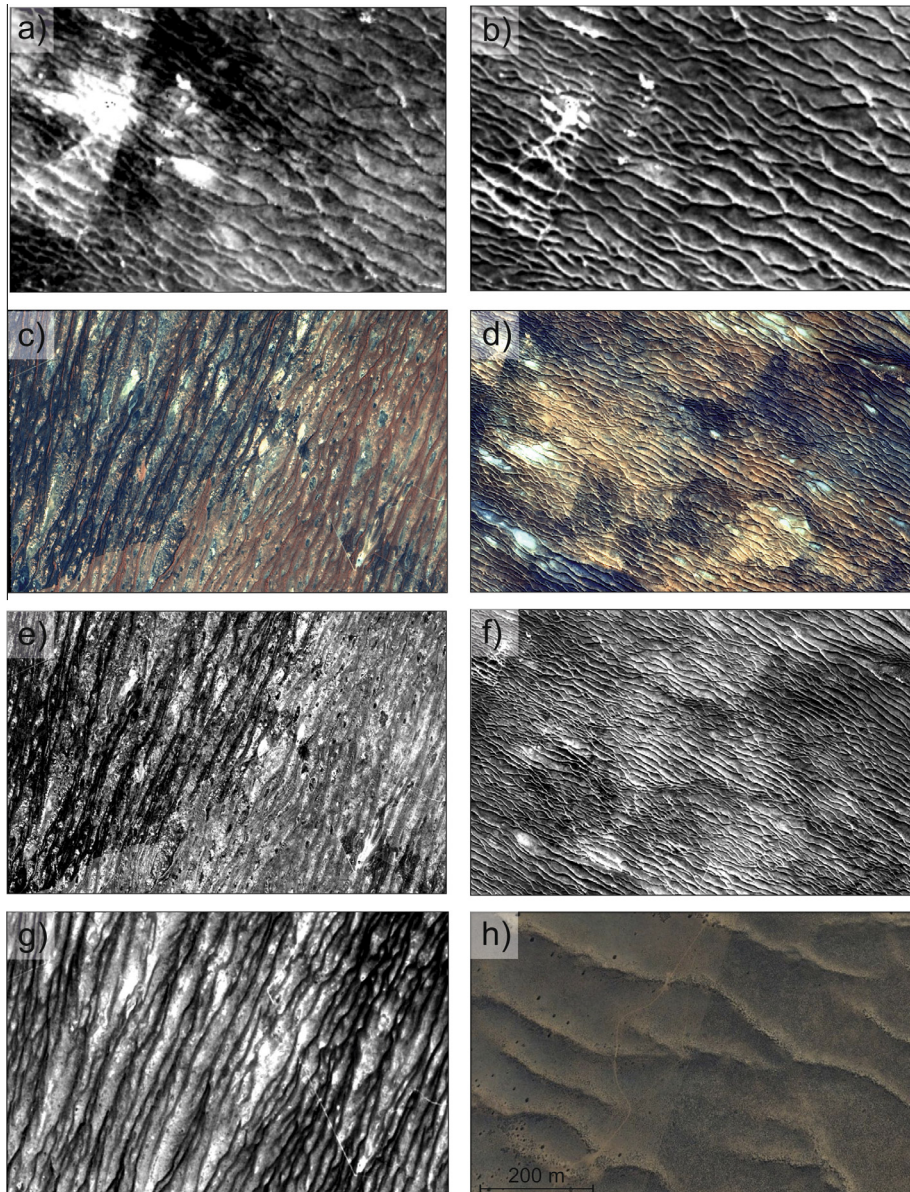


**Fig. 3.** Detail of the SW Kalahari South site reveals the significance of solar elevation in the choice of imagery for analysis. (a) Shows the panchromatic reflectance during summer (image taken 19 January 2014 08:34 GMT, with a solar elevation of  $59.0^\circ$  and azimuth of  $86.8^\circ$ ) compared to (b) winter imagery of the same scene (taken 27 May 2014 08:32 GMT, with a solar elevation  $34.4^\circ$  and azimuth  $34.7^\circ$ ). The challenges involved in delineating dune trends despite varied and sudden changes in vegetation cover are revealed in pan-sharpened RGB composites (Bands 2–4) for (c) the Strzelecki and (d) the SW Kalahari South sites. In the case of (e) the Strzelecki, this effect dominates any variance in reflectance due to the dunes, whereas in (f) the SW Kalahari South, the problem is less marked. (g) The Band 1 (deep blue-violet) image offers a possible solution to this problem, which is often the result of the effect of fencing on grazing patterns (h) (image courtesy of Google Earth™). (For interpretation of the references to colour in this figure legend, the reader is referred to the web version of this article.)

density is markedly different across the scene (Fig. 3c and d). This may be due to grazing intensity and the effects of fencing on the landscape (visible in high resolution SPOT imagery available on the Google Earth platform; Fig. 3h), or in the case of the Strzelecki site, due to fire which affected part of the site in September 2011 (Bastin and Allan, 2012). The panchromatic images for the two sites shown (Strzelecki: Fig. 3e; SW Kalahari South: Fig. 3f) reveal that the magnitude of this problem varies considerably. For the SW Kalahari South site, neighbourhood filtering is able to remove the effects of differing vegetation across the image. However at the Strzelecki site (Fig. 3c), spectral variance due to vegetation is much greater than the spectral difference that define the dune crests. Further investigation of the Strzelecki site, using imagery prior to the wildfires of 2011 (Landsat ETM

panchromatic Band 8, acquired 19th May 2003), however, reveals that at this location, dune crests are still not well defined, and the method described in Section 3.3 cannot be applied at this test site.

Further investigation of the spectral characteristics of the Strzelecki site, however, yielded an unexpected possibility for defining dunes on the basis of their spectral characteristics. Whilst bands in the infrared, and also Bands 3 (green) and 4 (red), were dominated by the vegetational changes, low reflectance in the blue (Band 2) and especially deep blue-violet (Band 1) are relatively unaffected by vegetation and delineate dunes very well (Fig. 3g). The reason for this is not immediately clear. Band 1 of the OLI is referred to informally as the 'Coastal/Aerosol' band, highlighting two of its most likely applications; the unusually short

wavelength for this type of sensor offers the potential for shallow water penetration, and is also particular suited for mapping the scattering caused by atmospheric aerosols (Irons et al., 2012). Variation in  $B$  and  $I$  appears therefore to be a function of the specularity of the dune surface, the moisture content of the dune sands compared to the interdunes, the nature of the vegetation or some other aspect of the dune surface. Understanding this would require further investigation beyond the scope of this paper.

### 3.3. Generalization

As noted in the methods section, a wide range of methods, of varying degrees of complexity, was tested with the eventual goal being the binary classification of scenes into dune/non-dune categories in a form most suitable for vectorization. Initial experimentation with the vectorization tools within ArcGIS revealed that the quality of the binary dune/non-dune input classification

was paramount in producing an accurate vectorization of the dune trends, and thus the focus of effort of this research was to produce the best possible input for vectorization.

Attempts with relatively simple methods met with some limited success. The dunes of the Great Sandy Desert site, which include complex patterning of the ridge crests (Fig. 4a) are broadly approximated by both a simple neighbourhood range filter with a radius of 1 pixel, or 15 m (Fig. 4b), and the difference between the raw image and a neighbourhood mean filter with a radius of 16 pixels, or 240 m (Fig. 4c). Similarly, the directionally-weighted kernel filter approach provided fair approximation of the overall outline of the dunes of the Simpson desert (Fig. 4e–f). Although noise-reduction methods, such as neighbourhood majority filters, improved output (Fig. 4g shows the data from Fig. 4f after noise-reduction via repeated majority filtering), closer inspection of all of the simpler approaches at all of the sites investigated (examples of detail for the Great Sandy and Simpson are shown in Fig. 4d

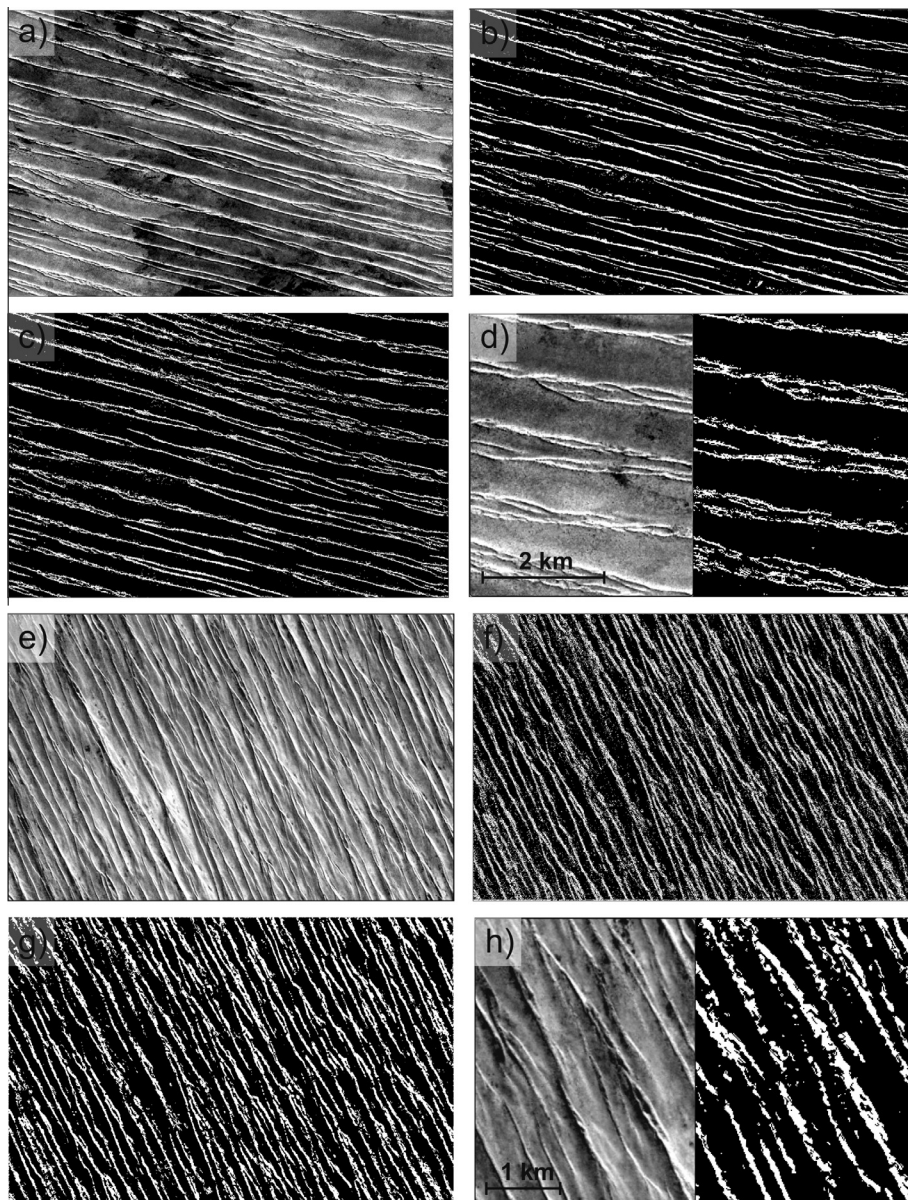


**Fig. 4.** (a) The complex crests of the dunes of the Great Sandy Desert appear fairly well-delimited with simple filters, such as (b) neighbourhood range and (c) high-pass/low-pass filter combinations, and (d) detail is lost to noise on closer inspection. (e) The dunes of the Simpson desert site are better represented with (f) a directionally weighted kernel filter, especially after (g) noise reduction via neighbourhood majority filtering, but again (h) close inspection reveals that details of dune topology are frequently lost. All scenes have a field of view  $15 \times 10$  km, unless scale is stated.

and  $h$  respectively) reveals that the more subtle aspects of dune morphology, especially intersections, are often lost amongst noise.

### 3.4. The Linear Dune Optimized (LIDO) edge detection algorithm

Initial experimentation with the Canny edge detection algorithm proved disappointing, and despite tuning the parameters of the method, the Canny routine tended to represent dunes as multiple and incomplete lines (Fig. 5a shows the Landsat panchromatic data, and Fig. 5b an example of Canny edge classification on this image). The method evidently had potential, however, as some subtle patterning was represented (Fig. 5c and d). Investigations of the component stages of the Canny algorithm showed that Gaussian blurring was causing, in some cases, a loss of fine detail amidst dunes with more complex patterning. The Sobel operators, however, were performing excellently in defining overall dune pattern and the failure of the method was occurring during the non-maxima suppression stage of the process. Essentially, in this application, the classification of the Sobel-derived image intensity gradient orientation into just four ordinal orientations discards useful directional information on the orientation of the dunes. From this basis, a Linear Dune-Optimized edge detection routine (LIDO) was established to exploit the advantages of the aspects of the Canny algorithm, which is shown in schematically in Fig. 6, and examples of the output are shown in Fig. 5e and f.

Firstly, a pair of  $5 \times 5$  Sobel operators in the  $x$  and  $y$  planes (with the  $y$  kernel having the form [1,4,6,4,1;2,8,12,8,2;0,0,0,0,0;−2,−8,−12,−8,−2;−1,−4,−6,−4,−1]) was used to derive the magnitude and direction of the image gradient for each pixel in the image. The use of a  $5 \times 5$  kernel provided some degree of smoothing within this operation, and was found to be preferable to the use of a prior Gaussian blur. Gradient magnitude and direction (in degrees) are derived from the kernel output such that:

$$G_M = \sqrt{S_x^2 + S_y^2} \quad (1)$$

$$G_D = (\text{atan}2(S_y, S_x) * 57.2958) + 180 \quad (2)$$

where  $G_M$  is the gradient magnitude,  $G_D$  the gradient direction,  $S_x$  is output of the Sobel  $x$ -operator and  $S_y$  is output of the Sobel  $y$ -operator.

Initially, very bright contiguous regions (where  $G_M > \mu_{GM} + 2\sigma_{GM}$ , where  $\mu_{GM}$  is the mean gradient magnitude of the whole dataset and  $\sigma_{GM}$  is the standard deviation of the dataset) were identified, and where the minimum radius of these zones exceeded 100 m, pixels were identified as pans (playas) and excluded from further classification as dunes (Fig. 5g and h). Examination of the histogram of  $G_D$  frequency across the image revealed a strongly bimodal distribution, with one peak corresponding to the dune trendlines. Pixels without a  $\pm 90^\circ$  range around this mode are assigned a gradient magnitude of zero. The size of the gradient magnitude is then used recursively to define 'strong' and 'weak' candidate dune pixels; at this stage, it was necessary to define a parameter ( $a$ ) to account for the variable amounts of noise in the different datasets. Strong candidates are defined as those pixels where  $G_M > \alpha\mu_{GM} + a\sigma_{GM}$  (where  $\alpha$  is a variable from 0 to 1), and weak pixels where  $G_M > \mu_{GM} + (a-0.25)\sigma_{GM}$ . Weak zones are accepted if they border (i.e. join) two or more separate strong zones. Candidate pixels are then zoned to enable the removal of small (<40 pixels, representing  $9000 \text{ m}^2$ ) areas. Vectorization was performed with ArcGIS's ArcScan tool with no gap closure, and ignoring 'holes' in the dunes with a diagonal length of less than 150 m. Lastly, vector line segments of less than 150 m which did not connect two or more dunes (i.e. spurs from the main crestlines) were removed. In both instances, the value of 150 m was derived empirically to reduce noise within the data whilst maintaining the key topological relationships.

### 3.5. Validation

To assess the performance of the LIDO algorithm in discerning dune trendlines, the vectorized output was compared to dune trendlines digitized from high-resolution Google Earth™ imagery. This was done manually, with attention focussed more towards ensuring correct topological relationships than spatial accuracy (e.g. a true positive would be recorded for a dune termination that was topologically correct but spatially inaccurate). For each type of pattern defect, successful matches were recorded from the LIDO output, along with false positives (i.e. defects detected by LIDO, but not by manual interpretation) and negative matches (i.e. defects detected manually, but missed by LIDO). From this, commonly used (e.g. Doucette et al., 2004) metrics of completeness, correctness and quality were derived such that:

$$\text{Correctness} = \text{TP}/(\text{TP} + \text{FP}) \quad (3)$$

$$\text{Completeness} = \text{TP}/(\text{TP} + \text{TN}) \quad (4)$$

$$\text{Quality} = \text{TP}/(\text{TP} + \text{FP} + \text{TN}) \quad (5)$$

where TP is the number of true positive detections, FP is the number of false positive detections and TN the number of true negative matches. The results are shown in Table 2.

Overall success with the LIDO algorithm for quantifying dune defects in linear dunefields is indicated with total defect quality metrics ranging from 0.68–0.84 for five of the six study sites. The panchromatic spectral characteristics of the Strzelecki site, both before and after the 2011 fires, did not allow for analysis using the LIDO algorithm, and further work is needed to discover why this region should have such markedly different spectral characteristics. Perhaps surprisingly, the dunefield with the most complex

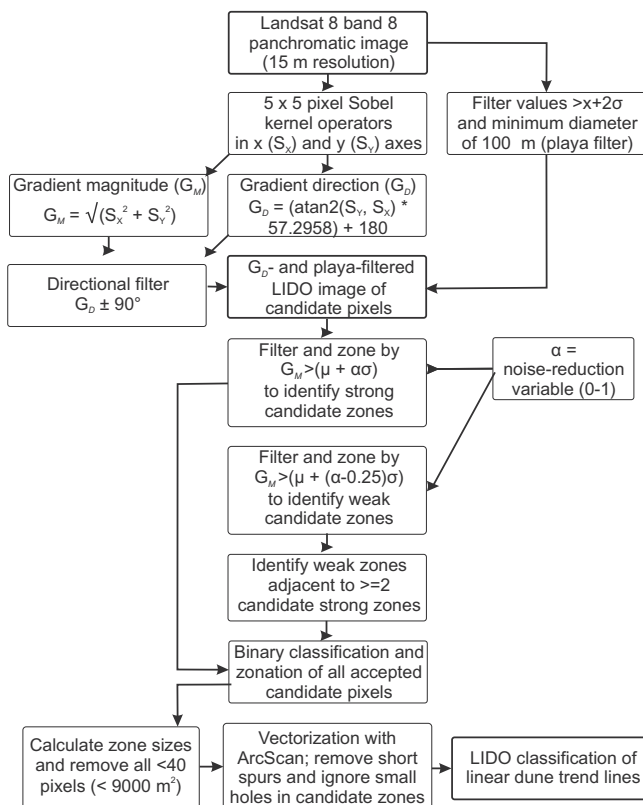
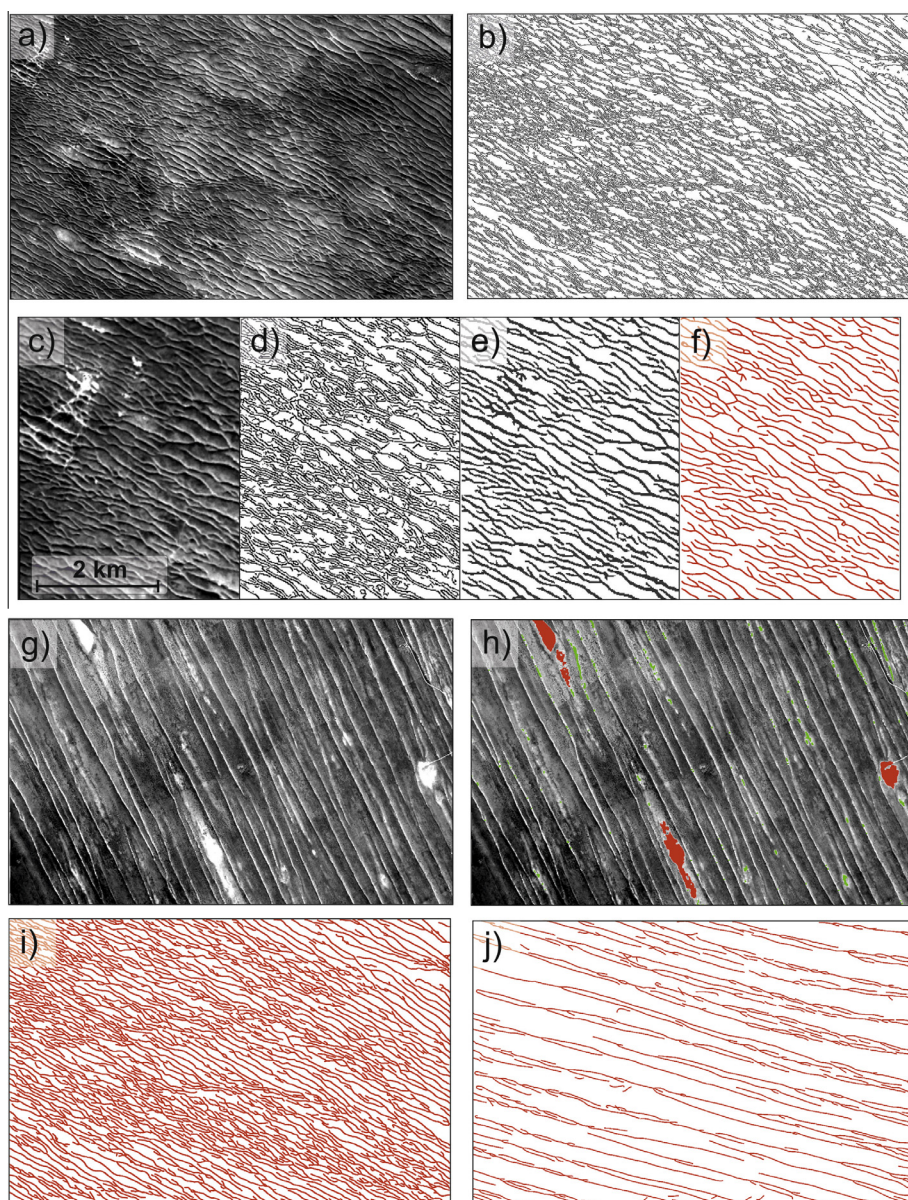


Fig. 5. Schematic of the Linear Dune Optimized (LIDO) edge detection routine.

patterning, the southern SW Kalahari, achieved the highest quality, and the northern SW Kalahari (which has the simplest patterning) ranked lowest in terms of overall quality. In all cases, completeness (i.e. identification of true positives) was substantially higher, and ranged from 0.90 to 0.97. The limitation to quality was primarily the identification of false positives, which in the case of the northern Kalahari site accounted for one third of total identified defects. Closer inspection of the false positive identification suggests that these are accounted for by three broad categories: (i) Minor limbs of dunes which were discounted during visual inspections, but which still exceeded the 150 m cut-off employed in the final stages, (ii) marginal dune junctions where topological relationships are debatable by visual inspection (e.g. Fig. 1) and (iii) Occasional misidentification of other features as dunes (for instance, in the Great Sandy, where marked interdune vegetational changes were wrongly identified as dune crests, evident in the southern edge of

Fig. 6j). In some cases (for instance a track in the northern SW Kalahari) the directionality of the filter was able to remove linear features with orientations very different to the local dune trend, but where this track turned parallel to the dunes, it was falsely identified as a dune. Although false positive identifications were fairly common in some areas, it was not possible to reduce the sensitivity of the algorithm further without loss of topological information.

Despite some differences between the manual interpretation and interpretation of the LIDO output, the method proposed here may thus provide a means of providing objectivity in delineating dune crests from remotely sensed data, which has been identified as a key challenge in the study of dunefield patterning (Hugenholtz et al., 2012). Occasional completely spurious identifications are likely (such as the above-mentioned track), but defining dune crests by quantitative spectral characteristics, minimum areal



**Fig. 6.** (a) The complex patterning of the southern SW Kalahari site illustrates the tendency of the Canny algorithm to produce double edges for the dune patterning (b) but also highlights the potential of Sobel-based algorithms for detecting subtle patterning. The insets show: (c) the raw Landsat8 image, (d) the Canny algorithm, (e) the LIDO raster classification and (f) the LIDO output vectorized with ArcScan. (g and h) Show an example of the playa filter detecting zones to be removed as dune candidates in red, and those bright areas to continue analysing in green. (i and j) Show the final LIDO vector output for the southern SW Kalahari site and the Great Sandy desert, respectively. All scenes have a field of view 15 × 10 km, unless scale is stated.

**Table 2**

Quantitative metrics of the performance of the LIDO algorithm in detecting defects within linear dune patterning.

Site name	Observed	Total detected	True positive	False positive	Negative	Correctness	Completeness	Quality
<i>Total defects</i>								
Kalahari North	37	52	36	16	1	0.69	0.97	0.68
Kalahari Central	79	94	71	23	8	0.76	0.90	0.70
Kalahari South	954	1005	894	111	60	0.89	0.94	0.84
Great Sandy Desert	285	335	254	81	20	0.76	0.93	0.72
Simpson	128	159	124	35	4	0.78	0.97	0.76
Strzelecki	119	n/a	n/a	n/a	n/a	n/a	n/a	n/a
<i>Start terminations</i>								
Kalahari North	20	27	20	7	0	0.74	1.00	0.74
Kalahari Central	31	37	29	8	2	0.78	0.94	0.74
Kalahari South	456	458	422	36	34	0.92	0.93	0.86
Great Sandy Desert	152	182	140	42	12	0.77	0.92	0.72
Simpson	61	76	61	15	0	0.80	1.00	0.80
Strzelecki	58	n/a	n/a	n/a	n/a	n/a	n/a	n/a
<i>End terminations</i>								
Kalahari North	13	20	12	8	1	0.60	0.92	0.57
Kalahari Central	15	22	14	8	1	0.64	0.93	0.61
Kalahari South	181	181	163	18	18	0.90	0.90	0.82
Great Sandy Desert	16	18	13	5	3	0.72	0.81	0.62
Simpson	17	22	17	5	0	0.77	1.00	0.77
Strzelecki	17	n/a	n/a	n/a	n/a	n/a	n/a	n/a
<i>Open junctions</i>								
Kalahari North	0	1	0	1	0	0.00	0.00	0.00
Kalahari Central	4	0	0	0	4	0.00	0.00	0.00
Kalahari South	60	58	55	3	5	0.95	0.92	0.87
Great Sandy Desert	15	19	13	6	1	0.68	0.93	0.65
Simpson	3	2	2	0	1	1.00	0.67	0.67
Strzelecki	8	n/a	n/a	n/a	n/a	n/a	n/a	n/a
<i>Closed junctions</i>								
Kalahari North	4	4	4	0	0	1.00	1.00	1.00
Kalahari Central	29	35	28	7	1	0.80	0.97	0.78
Kalahari South	257	308	254	54	3	0.82	0.99	0.82
Great Sandy Desert	102	116	88	28	4	0.76	0.96	0.73
Simpson	47	59	44	15	3	0.75	0.94	0.71
Strzelecki	36	n/a	n/a	n/a	n/a	n/a	n/a	n/a

extent and minimum lengths offers the critical advantage of removing many of the subjective aspects of aerial image interpretation when marginal decisions must be made where topological relationships are not clear. For instance, the lower quality metrics for the relatively simple patterning of the northern Kalahari site are in large part due to the LIDO algorithm including more subsidiary dunes of >150 m length which manual interpretation tended to overlook. It might be that this is due to their apparent visual insignificance during manual interpretation, as they abut the large, well-spaced dunes that characterize the northern Kalahari.

Although, globally, stabilized linear dunefields bear remarkable similarity in scale across a range of continents, the values arrived at in this study for minimum pan size (200 m diameter) and minimum dune length (150 m) may merit further investigation, and it is not necessarily the case that these values will be optimal for all dunefields. Nonetheless, the number of adjustable parameters necessary for this algorithm is minimal, and such experimentation should prove straightforward; it would be prudent to validate the method with further test sites if the method is to be applied to a new dunefield. Furthermore, some issues not encountered in this study are likely to need resolution before the method can be up-scaled to the dunefield scale. All of the dunefields tested here are larger than individual Landsat8 scenes, and thus mosaicking will be required prior to analysis, with attention paid to edge effects. The variability in reflectance characteristics evident between and within dunefields, also suggests that care will need to be taken to ensure that images are as comparable as possible (for instance, where possible, consecutive scenes along the satellite path).

Currently, the assumption is made of homogenous dune trend orientation within the image from which to derive  $G_D$  and of consistent noise from which to estimate an appropriate value for the variable  $\alpha$ . This is unlikely to be the case at larger scales, and certainly in the southwestern Kalahari dune orientation varies from N-S to almost E-W. At the dunefield scale, it will be necessary to analyze subsections, perhaps best defined by regions of near-consistent dune orientation and methods for successfully defining these areas and merging analyses will require consideration.

Although the algorithm has not currently been tested on other dune morphologies, there is scope for wider application. The method should work equally well on transverse dunes, and should be applicable where such dunes are abundant; the Transverse Aeolian Ridges (TARs) of Mars are an obvious possibility. Freely available and downloadable spectral data, such as that provided by the HiRISE sensor of the Mars Reconnaissance Orbiter, is of a higher spatial resolution (in many cases, 25 cm) than that of free terrestrial spatial data, and the approach presented here may aid in analysis of aeolian bedforms on Mars and other planetary settings. Dunes with wider variations in crest orientation (e.g. star dunes and barchans) are unlikely to be well-represented. It has been noted that the method worked most successfully where the background noise introduced by vegetation is minimal, and thus although the focus of this paper has been on semi-arid and vegetated dunefields, there is scope for applying the methodologies proposed herein to mapping and monitoring of fully active linear dunes in fully arid regimes.

#### 4. Conclusion

After testing a range of edge-detection methods on DEM and spectral data, a method has been derived which is able to delineate dune trend lines in linear dunefields with a high degree of completeness (0.86–0.99) and an acceptable level of overall quality (0.68–0.84). At present, freely available elevation data (Aster GDEM v2 and 1 arc-second SRTM) are only able to adequately represent the topology of dunes which are typically <10 m in height where this patterning is relatively simple. High-resolution (15 m) panchromatic data from Landsat 8, however, typically represents dune crests as sharp breaks in reflectance which can be identified with edge-detection routines. A methodology refined for the identification of linear dunes is proposed here, which uses Sobel operators as the core of the edge detection algorithm and exploits the preferred orientation of image gradient direction associated with linear dunes.

The successful semi-automated delineation of dune trend lines in linear dunefields offers potential in several aspects of research. Applied to entire regions of semi-active dunes (which occupy, for instance, the majority of central Australia, central southern Africa and large parts of the Chinese deserts), the possibility of readily quantifying pattern metrics at a large scale exists for the first time. Such information is likely to be essential in providing validation data for understanding the boundary conditions that control dunefield evolution (Ewing and Kocurek, 2010; Telfer and Hesse, 2013), which currently hampers understanding of dune geomorphology. The ability to relatively quickly survey and re-survey at a large scale also offers the potential for assessing the temporal evolution of linear dunefields. Whether or not linear dunefields are at risk of widespread remobilization under the influence of 21st century climate change is a debated point (Thomas et al., 2005; Wang et al., 2009), and the ability to efficiently monitor dunefield change at ~10 m scale offers a valuable tool in detecting early evidence of reactivation and mobilization of the world's stabilized dunefields.

#### Acknowledgments

ASTER GDEM is a product of METI and NASA. Landsat 8 data are distributed by the Land Processes Distributed Active Archive Center (LP DAAC), located at USGS/EROS, Sioux Falls, SD (<http://lpdaac.usgs.gov>). Colleagues at the 8th International Conference on Aeolian Research in Lanzhou, China, July 2014 are thanked for constructive comments on the development of the methodology of this paper, and the University of Plymouth is thanked for funding the attendance of MT at this meeting. Two anonymous referees are thanked for their comments which have improved this paper.

#### References

- Al-Dabi, H., Koch, M., Al-Sarawi, M., El-Baz, F., 1997. Evolution of sand dune patterns in space and time in north-western Kuwait using Landsat images. *J. Arid Environ.* 36, 15–24.
- Al-Masrahy, M.A., Mountney, N.P., 2013. Remote sensing of spatial variability in aeolian dune and interdune morphology in the Rub' Al-Khali, Saudi Arabia. *Aeolian Res.* 11, 155–170.
- Athmania, D., Achour, H., 2014. External validation of the ASTER GDEM2, GMTED2010 and CGIAR-CSI-SRTM v4.1 Free Access Digital Elevation Models (DEMs) in Tunisia and Algeria. *Remote Sens.* 6, 4600–4620.
- Bastin, G., Allan, G., 2012. After the smoke has cleared: 2011 fire in central Australia. *Rangeland Manage. Newsletter* 12, 3–6.
- Bubenzer, O., Bolten, A., 2008. The use of new elevation data (SRTM/ASTER) for the detection and morphometric quantification of Pleistocene megadunes (draa) in the eastern Sahara and the southern Namib. *Geomorphology* 102, 221–231.
- Bullard, J.E., Thomas, D.S.G., Livingstone, I., Wiggs, G.F.S., 1995. Analysis of linear sand dune morphological variability, southwestern Kalahari Desert. *Geomorphology* 11, 189–203.
- Canny, J., 1986. A computational approach to edge detection. *IEEE Trans. Pattern Anal. Mach. Intell.*, 679–714.
- Cazenave, P.W., Dix, J.K., Lambkin, D.O., McNeill, L.C., 2013. A method for semi-automated objective quantification of linear bedforms from multi-scale digital elevation models. *Earth Surf. Processes Landforms* 38, 221–236.
- Derickson, D., Kocurek, G., Ewing, R.C., Bristow, C., 2008. Origin of a complex and spatially diverse dune-field pattern, Algodones, southeastern California. *Geomorphology* 99, 186–204.
- Dong, Z.B., Wei, Z.H., Qian, G.Q., Zhang, Z.C., Luo, W.Y., Hu, G.Y., 2010. "Raked" linear dunes in the Kumtagh Desert, China. *Geomorphology* 123, 122–128.
- Doucette, P., Agouris, P., Stefanidis, A., 2004. Automated road extraction from high resolution multispectral imagery. *Photogramm. Eng. Remote Sens.* 70, 1405–1416.
- Ewing, R.C., Kocurek, G., 2010. Aeolian dune-field pattern boundary conditions. *Geomorphology* 114, 175–187.
- Ewing, R.C., Kocurek, G., Lake, L.W., 2006. Pattern analysis of dune-field parameters. *Earth Surf. Processes Landforms* 31, 1176–1191.
- Fitzsimmons, K.E., 2007. Morphological variability in the linear dunefields of the Strzelecki and Tirari Deserts, Australia. *Geomorphology* 91, 146–160.
- Hesse, P.P., 2010. The Australian desert dunefields: formation and evolution in an old, flat, dry continent. In: Bishop, P., Pillans, B. (Eds.), *Australian Landscapes*. Geological Society Publishing House, Bath, pp. 141–164.
- Hesse, P.P., Simpson, R.L., 2006. Variable vegetation cover and episodic sand movement on longitudinal desert sand dunes. *Geomorphology* 81, 276–291.
- Hugenholz, C.H., Barchyn, T.E., 2010. Spatial analysis of sand dunes with a new global topographic dataset: new approaches and opportunities. *Earth Surf. Processes Landforms* 35, 986–992.
- Hugenholz, C.H., Levin, N., Barchyn, T.E., Baddock, M.C., 2012. Remote sensing and spatial analysis of aeolian sand dunes: a review and outlook. *Earth Sci. Rev.* 111, 319–334.
- Irons, J.R., Dwyer, J.L., Barsi, J.A., 2012. The next Landsat satellite: the Landsat Data Continuity Mission. *Remote Sens. Environ.* 122, 11–21.
- Kocurek, G., Ewing, R.C., Mohrig, D., 2010. How do bedform patterns arise? New views on the role of bedform interactions within a set of boundary conditions. *Earth Surf. Processes Landforms* 35, 51–63.
- Krieger, G., Moreira, A., Fiedler, H., Hajnsek, I., Werner, M., Younis, M., Zink, M., 2007. TanDEM-X: a satellite formation for high-resolution SAR interferometry. *IEEE Trans. Geosci. Remote Sens.* 45, 3317–3341.
- Lancaster, N., 1995. *Geomorphology of desert dunes*. Routledge, Physical Environment Series.
- Lancaster, N., Kocurek, G., Singhvi, A., Pandey, V., Deynoux, M., Ghienne, J.F., Lo, K., 2002. Late Pleistocene and Holocene dune activity and wind regimes in the western Sahara Desert of Mauritania. *Geology* 30, 991–994.
- NASA/METI, 2011. ASTER Global Digital Elevation Model (GDEM) ver. 2.
- Sobel, I., Feldman, G., 1968. A 3x3 Isotropic Gradient Operator for Image Processing, Stanford Artificial Intelligence Project (SAIL), Stanford.
- Tachikawa, T., Kaku, M., Iwasaki, A., Gesch, D., Omoen, M., Zhang, Z., Danielson, J., Krieger, T., Curtis, B., Haase, J., Abrams, M., Craven, R., Carabajal, C., 2011. ASTER Global Digital Elevation Model Version 2 – Summary of Validation Results. In: Meyer, D. (Ed.), *NASA Land Processes Distributed Active Archive Center and the Joint Japan-US ASTER Science Team*.
- Telfer, M.W., Hesse, P.P., 2013. Palaeoenvironmental reconstructions from linear dunefields: recent progress, current challenges and future directions. *Quat. Sci. Rev.* 78, 1–21.
- Thomas, D.S.G., Knight, M., Wiggs, G.F.S., 2005. Remobilization of southern African desert dune systems by twenty-first century global warming. *Nature* 435, 1218.
- Thomas, D.S.G., Shaw, P.A., 1991. *The Kalahari Environment*. Cambridge University Press, Cambridge.
- Varma, G.S., Banerjee, B., Mohan, B.K., 2012. Representation of desert sand dunes by surface orientations using Radon transform 2012. In: *IEEE International Geoscience and Remote Sensing Symposium*. IEEE, New York, pp. 2733–2736.
- Varma, S., Shah, V., Banerjee, B., Buddhiraju, K.M., 2014. Change detection of Desert Sand Dunes: a remote sensing approach. *Adv. Remote Sens.*, 10–22.
- Wang, X.M., Yang, Y., Dong, Z.B., Zhang, C.X., 2009. Responses of dune activity and desertification in China to global warming in the twenty-first century. *Global Planet. Change* 67, 167–185.
- Werner, B.T., 1995. Aeolian dunes: computer simulations and attractor interpretations. *Geology* 23, 1107–1110.
- Werner, B.T., Kocurek, G., 1997. Bed-form dynamics: does the tail wag the dog? *Geology* 25, 771–774.
- Werner, B.T., Kocurek, G., 1999. Bedform spacing from defect dynamics. *Geology* 27, 727–730.